Supplementary information:
An Open-Source Framework for Quantitative Electrostatic Simulations in Kelvin Probe Force Microscopy

Nobuyuki Ishida[1]

[1]*National Institute for Materials Science, 1-2-1 Sengen, Tsukuba, Ibaraki 305-0047, Japan*

I. SUPPLEMENTARY NOTE I: NUMERICAL IMPLEMENTATION OF METALTIP IN GENERALIZED PROLATE SPHEROIDAL COORDINATES

This Supplementary Note provides a complete description of the numerical implementation of METALTIP, including the coordinate definitions, parameter relations, discretization scheme, boundary conditions, and solver procedures. The overall computational strategy largely follows the SEMITIP framework developed by Feenstra [1–6].

A. Generalized prolate spheroidal coordinates

In METALTIP, following the SEMITIP framework, the vacuum region between the tip and the sample is described using a generalized prolate spheroidal coordinate system (ξ, η). A key advantage of this coordinate choice is that the tip boundary can be aligned with a coordinate surface, $\eta = \eta_T$, which allows the boundary condition on the tip to be imposed straightforwardly while retaining a compact grid representation of a sharp apex and the vacuum gap.

The generalized coordinates (ξ, η) are defined in the (r, z) cross-section of the cylindrical coordinate system, where r is the radial coordinate and z is the axial coordinate, by the implicit relations

$$\frac{r^2}{\xi^2 - 1} + \frac{(z - ac\,\eta)^2}{\xi^2} = a^2, \tag{1}$$

$$\frac{r^2}{1 - \eta^2} + \frac{(z - ac\,\eta)^2}{\eta^2} = a^2, \tag{2}$$

where a sets the characteristic length scale of the mapping (equal to the focal length in the standard prolate spheroidal system) and c is a dimensionless parameter introduced in the generalized formulation. Introducing c adds geometric flexibility: it allows the tip surface to coincide with a coordinate surface while enabling the tip–sample separation (vacuum gap) to be tuned independently, as detailed in Sec. I B. Surfaces of constant ξ and constant η correspond to spheroidal (ellipsoidal) and hyperboloidal quadric surfaces, respectively (see Fig. S1).

Solving Eqs. (1) and (2) for (r, z) yields an explicit mapping to the physical space in

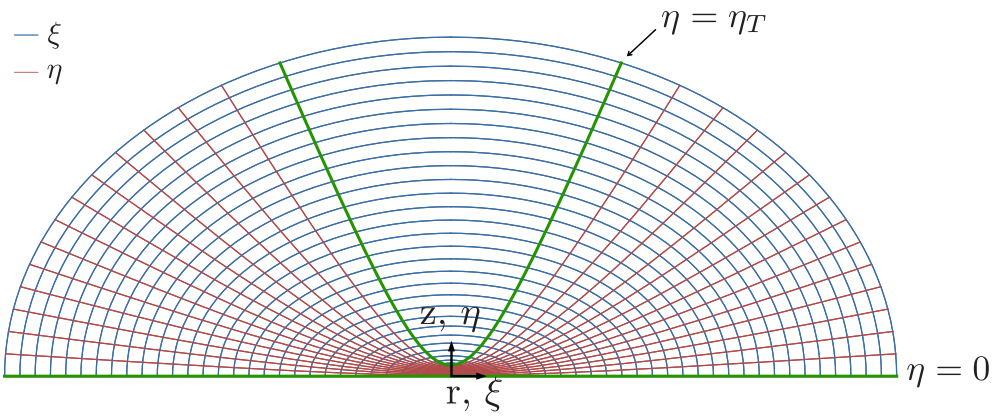

FIG. S1: Example of the grid in the generalized prolate spheroidal coordinates (ξ, η) used in SEMITIP/METALTIP. The ξ = const. and η = const. lines form spheroidal and hyperboloidal families, respectively. For $c \neq 0$ the coordinates are generally non-orthogonal.

Alt text: Coordinate grid used in SEMITIP/METALTIP. Lines of constant ξ and η form spheroidal and hyperboloidal coordinate families, and the generalized coordinate system is non-orthogonal when $c \neq 0$.

cylindrical coordinates:

$$r(\xi, \eta) = a\sqrt{(\xi^2 - 1)(1 - \eta^2)}, \tag{3}$$

$$z(\xi, \eta) = a(\xi + c)\eta. \tag{4}$$

With this definition, the sample surface coincides with $\eta = 0$ (i.e., $z = 0$). The tip boundary is represented by choosing a coordinate surface, $\eta = \eta_T$, to coincide with the tip surface. The definition of η_T in terms of the tip geometric parameters is summarized in Sec. I B.

Figure S1 shows a representative grid of the generalized prolate spheroidal coordinates used in METALTIP. Unlike the standard (orthogonal) prolate spheroidal coordinates, the present generalized system with $c \neq 0$ is generally non-orthogonal; the coordinate lines of constant ξ and constant η are not mutually perpendicular in the (r, z) cross-section. This non-orthogonality introduces mixed ξ–η terms in the Laplacian (see Sec. I E), while retaining a compact grid in the near-apex region where the electrostatic field is strongly localized.

B. Determination of the tip boundary parameter η_T

The tip is modeled as a rotationally symmetric hyperboloid, specified by the tip radius R, the full opening angle α, and the tip–sample separation s. Note that η_T is determined solely by the opening angle α, whereas R sets the scale parameter a and s sets the shift parameter c.

We define the shank-slope parameter as the asymptotic slope in the (r, z) cross-section,

$$b \equiv \left.\frac{dz}{dr}\right|_{\text{asym}} = \cot\left(\frac{\alpha}{2}\right). \tag{5}$$

The tip surface is aligned with the coordinate surface $\eta = \eta_T$, where

$$\eta_T = \frac{1}{\sqrt{1 + b^{-2}}} = \cos\left(\frac{\alpha}{2}\right). \tag{6}$$

The scale parameter a is determined by requiring the local apex curvature to match R,

$$a = \frac{Rb^2}{\eta_T}. \tag{7}$$

Defining $s' \equiv a\eta_T$, the vertical shift is chosen such that the apex position corresponds to the prescribed separation s:

$$z_0 = s - s', \qquad c = \frac{z_0}{a\eta_T} = \frac{s}{a\eta_T} - 1. \tag{8}$$

These relations ensure that the coordinate surface $\eta = \eta_T$ coincides with the hyperbolic tip boundary and that the apex point $(\xi, \eta) = (1, \eta_T)$ is mapped to $(r, z) = (0, s)$ with the desired local curvature R.

C. Grid construction and indexing

The η coordinate is discretized uniformly between the sample plane ($\eta = 0$) and the tip surface ($\eta = \eta_T$) with

$$\Delta\eta = \frac{\eta_T}{N_v}. \tag{9}$$

The interior vacuum nodes are indexed as $j = 0, 1 \ldots, N_v - 1$ and are placed at

$$\eta_j = (j + 1)\,\Delta\eta, \qquad (j = 0, 1, \ldots, N_v - 1). \tag{10}$$

The sample surface at $\eta = 0$ is not included as a grid point; the first vacuum node is located at $\eta = \Delta\eta$.

To maintain high resolution near the axis while keeping a sufficiently large lateral domain, we introduce a variable (non-uniform) grid in the radial direction using a tangent-type mapping,

$$r_i = \frac{2N_r \Delta r}{\pi} \tan\left[\frac{\pi}{2N_r}\left(i + \frac{1}{2}\right)\right], \qquad (i = 0, 1, \ldots, N_r - 1), \tag{11}$$

where Δr controls the near-axis spacing. Note that the central axis at $r = 0$ (corresponding to $\xi = 1$) is not included as a grid point. The corresponding ξ_i values are determined from the sample-plane relation at $\eta = 0$,

$$\xi_i = \sqrt{1 + \left(\frac{r_i}{a}\right)^2}. \tag{12}$$

Once $\{\xi_i\}$ and $\{\eta_j\}$ are defined, the physical-space grid points follow from Eqs. (3) and (4). In particular, the radial and vertical coordinates at a general grid point (i, j) are given by

$$r_{ij} = a\sqrt{(\xi_i^2 - 1)(1 - \eta_j^2)} = r_i\sqrt{1 - \eta_j^2}, \tag{13}$$

$$z_{ij} = a(\xi_i + c)\eta_j = a\eta_j\left(\sqrt{1 + \left(\frac{r_i}{a}\right)^2} + c\right). \tag{14}$$

For the three-dimensional (3D) solver, an azimuthal angle θ is introduced and discretized uniformly,

$$\theta_k = k\,\Delta\theta, \qquad \Delta\theta = \frac{2\pi}{N_p}, \qquad k = 0, 1, \ldots, N_p - 1, \tag{15}$$

with periodic boundary conditions identifying $\theta_{-1} \equiv \theta_{N_p-1}$ and $\theta_{N_p} \equiv \theta_0$.

D. Boundary conditions

The boundary conditions are specified as follows:

1. Sample surface ($\eta = 0$): the surface potential is prescribed as a Dirichlet boundary condition,

$$\phi(\xi, \eta = 0, \theta) = V_s(\xi, \theta). \tag{16}$$

   Here $V_s(\xi, \theta)$ denotes the surface potential defined on the $\eta = 0$ plane, i.e., $V_s(\xi, \theta) \equiv V_s(r(\xi, 0), \theta)$. For the 2D calculations, we assume a grounded sample ($V_s = 0$).

2. Tip surface ($\eta = \eta_T$): the tip is treated as an ideal conductor at the applied bias U,

$$\phi(\xi, \eta = \eta_T, \theta) = U. \tag{17}$$

3. Symmetry axis ($r = 0$, $\xi = 1$): axial symmetry yields the Neumann condition,

$$\left.\frac{\partial \phi}{\partial r}\right|_{r=0} = 0. \tag{18}$$

4. Outer boundary ($\xi = \xi_{\max}$): the outer boundary is placed sufficiently far from the apex, and a homogeneous Neumann-type condition is imposed in the ξ direction.

$$\left.\frac{\partial \phi}{\partial \xi}\right|_{\xi=\xi_{\max}} = 0. \tag{19}$$

As mentioned in Section I C, the plane $\eta = 0$ is not explicitly included as computational nodes; the Dirichlet condition on the sample is therefore enforced using a ghost layer adjacent to the first vacuum layer. In particular, when updating the first vacuum layer ($j = 0$, $\eta = \Delta\eta$), the surface Dirichlet condition is applied by assigning the prescribed value V_s as a ghost value at $j = -1$.

The symmetry axis $\xi = 1$ ($r = 0$) is a coordinate singularity and is not explicitly included in the grid. Regularity at the axis requires that the potential remain finite. Accordingly, the axis condition is enforced in a finite-difference sense by introducing an on-axis ghost value obtained from a short extrapolation stencil. In practice, the on-axis potential is evaluated from the nearest off-axis points (e.g., $i = 0$ and $i = 1$) as

$$\phi_{\mathrm{ax},j,k} \approx \frac{9}{8}\phi_{0,j,k} - \frac{1}{8}\phi_{1,j,k}, \tag{20}$$

which is consistent with $\left.\partial\phi/\partial r\right|_{r=0} = 0$.

E. Discretization of the Laplace equation in the generalized (ξ, η) coordinates

In the vacuum region, the electrostatic potential ϕ satisfies Laplace equation, $\nabla^2\phi = 0$. In the generalized prolate spheroidal coordinates (ξ, η, θ), this equation can be written as the following second-order partial differential equation:

$$f_1(\xi,\eta)\frac{\partial^2\phi}{\partial\xi^2} + f_2(\xi,\eta)\frac{\partial^2\phi}{\partial\eta^2} + f_3(\xi,\eta)\frac{\partial^2\phi}{\partial\theta^2} + f_4(\xi,\eta)\frac{\partial^2\phi}{\partial\xi\,\partial\eta} + f_5(\xi,\eta)\frac{\partial\phi}{\partial\xi} + f_6(\xi,\eta)\frac{\partial\phi}{\partial\eta} = 0, \tag{21}$$

where the coefficient functions $f_n(\xi,\eta)$ are given by

$$f_1(\xi,\eta) = \frac{(\xi^2-1)\left[(\xi+c)^2-\eta^2(2c\xi+c^2+1)\right]}{\xi(\xi+c)-\eta^2(c\xi+1)}, \tag{22}$$

$$f_2(\xi,\eta) = \frac{(1-\eta^2)(\xi^2-\eta^2)}{\xi(\xi+c)-\eta^2(c\xi+1)}, \tag{23}$$

$$f_3(\xi,\eta) = \frac{\xi(\xi+c)-\eta^2(c\xi+1)}{(\xi^2-1)(1-\eta^2)}, \tag{24}$$

$$f_4(\xi,\eta) = \frac{-2c\eta(\xi^2-1)(1-\eta^2)}{\xi(\xi+c)-\eta^2(c\xi+1)}, \tag{25}$$

$$f_5(\xi,\eta) = \frac{g_5(\xi,\eta)}{\left[\xi(\xi+c)-\eta^2(c\xi+1)\right]^2}, \tag{26}$$

$$f_6(\xi,\eta) = \frac{g_6(\xi,\eta)}{\left[\xi(\xi+c)-\eta^2(c\xi+1)\right]^2}, \tag{27}$$

with

$$\begin{aligned} g_5(\xi,\eta) = {} & c^3+3c^2\xi+c(2+c^2)\xi^2+3c^2\xi^3+4c\xi^4+2\xi^5 \\ & +\eta^4\left[c^3+(2+3c^2)\xi+c(6+c^2)\xi^2+3c^2\xi^3\right] \\ & -2\eta^2\left[c(c^2-1)+3c^2\xi+c(6+c^2)\xi^2+(2+3c^2)\xi^3+c\xi^4\right], \end{aligned} \tag{28}$$

$$\begin{aligned} g_6(\xi,\eta) = {} & -\eta\Big\{c^2+4c\xi+c^2\xi^2+2\xi^4+\eta^4\left[2+c^2+4c\xi+c^2\xi^2\right] \\ & -2\eta^2\left[c^2+4c\xi+(2+c^2)\xi^2\right]\Big\}. \end{aligned} \tag{29}$$

Under axial symmetry, ϕ is independent of the azimuthal angle θ, so that $\partial\phi/\partial\theta = 0$ and the θ-derivative term vanishes, i.e., $f_3(\xi,\eta)\,\partial^2\phi/\partial\theta^2 = 0$. The vacuum problem is then reduced to a two-variable equation in (ξ,η). In the generalized system ($c \neq 0$), the mixed ξ–η term remains.

Equation (21) is discretized on the (ξ,η,θ) grid using *second-order* finite differences. The η and θ directions use uniform spacings $\Delta\eta$ and $\Delta\theta$, whereas the ξ direction follows the non-uniform grid described in Sec. I C. We define the local ξ spacings as

$$\Delta\xi_i^- \equiv \xi_i - \xi_{i-1}, \qquad \Delta\xi_i^+ \equiv \xi_{i+1} - \xi_i, \qquad \Delta\xi_i \equiv \Delta\xi_i^- + \Delta\xi_i^+. \tag{30}$$

At the symmetry axis, $\xi = 1$ is treated as a ghost boundary; in the implementation, $\Delta\xi_0^-$ is taken as the distance from $\xi = 1$ to ξ_0.

The discrete equation at an interior vacuum node (i,j,k) can be written as a weighted

sum of neighboring values (a *stencil*):

$$A^+_{ij}\phi_{i+1,j,k} + A^-_{ij}\phi_{i-1,j,k} + B^+_{ij}\phi_{i,j+1,k} + B^-_{ij}\phi_{i,j-1,k} + C_{ij}(\phi_{i+1,j+1,k} - \phi_{i+1,j-1,k} - \phi_{i-1,j+1,k} + \phi_{i-1,j-1,k}) + P_{ij}\,(\phi_{i,j,k+1} + \phi_{i,j,k-1}) - D_{ij}\phi_{i,j,k} = 0. \tag{31}$$

where the coefficients are

$$A^+_{ij} = f_1(\xi_i,\eta_j)\,\frac{2}{\Delta\xi^+_i\Delta\xi_i} + f_5(\xi_i,\eta_j)\,\frac{1}{\Delta\xi_i}, \tag{32}$$

$$A^-_{ij} = f_1(\xi_i,\eta_j)\,\frac{2}{\Delta\xi^-_i\Delta\xi_i} - f_5(\xi_i,\eta_j)\,\frac{1}{\Delta\xi_i}, \tag{33}$$

$$B^+_{ij} = f_2(\xi_i,\eta_j)\,\frac{1}{\Delta\eta^2} + f_6(\xi_i,\eta_j)\,\frac{1}{2\Delta\eta}, \tag{34}$$

$$B^-_{ij} = f_2(\xi_i,\eta_j)\,\frac{1}{\Delta\eta^2} - f_6(\xi_i,\eta_j)\,\frac{1}{2\Delta\eta}, \tag{35}$$

$$C_{ij} = f_4(\xi_i,\eta_j)\,\frac{1}{2\,\Delta\eta\,\Delta\xi_i}, \tag{36}$$

$$P_{ij} = f_3(\xi_i,\eta_j)\,\frac{1}{\Delta\theta^2}, \tag{37}$$

$$D_{ij} = \left(A^+_{ij} + A^-_{ij}\right) + \left(B^+_{ij} + B^-_{ij}\right) + 2P_{ij}. \tag{38}$$

For numerical efficiency, these coefficients are precomputed and stored in the code as Ap$=A^+$, Am$=A^-$, Bp$=B^+$, Bm$=B^-$, C$=C$, P$=P$, and inv_den$=1/D$.

Equation (31) is solved iteratively using Gauss–Seidel iteration with successive over-relaxation (SOR). At each iteration (sweep), the interior vacuum nodes are updated in place (i.e., array entries are overwritten during the sweep). We first compute the Gauss–Seidel estimate by rearranging Eq. (31) as

$$\phi^{\mathrm{GS}}_{i,j,k} = \mathrm{inv\_den}_{ij}\Big[\mathrm{Ap}_{ij}\phi_{i+1,j,k} + \mathrm{Am}_{ij}\phi_{i-1,j,k} + \mathrm{Bp}_{ij}\phi_{i,j+1,k} + \mathrm{Bm}_{ij}\phi_{i,j-1,k} + \mathrm{C}_{ij}(\phi_{i+1,j+1,k} - \phi_{i+1,j-1,k} - \phi_{i-1,j+1,k} + \phi_{i-1,j-1,k}) + \mathrm{P}_{ij}\,(\phi_{i,j,k+1} + \phi_{i,j,k-1})\Big], \tag{39}$$

and then apply SOR,

$$\phi_{i,j,k} \leftarrow (1-\omega)\,\phi_{i,j,k} + \omega\,\phi^{\mathrm{GS}}_{i,j,k}, \tag{40}$$

where ω is the over-relaxation factor. Dirichlet boundary nodes are excluded from the updates. The iteration is continued until the maximum change in ϕ between successive

sweeps falls below a prescribed tolerance,

$$\max_{i,j,k} \left| \phi_{i,j,k}^{(n+1)} - \phi_{i,j,k}^{(n)} \right| < \varepsilon_\phi. \tag{41}$$

To improve numerical accuracy while keeping the computational cost manageable, we employ a staged grid-refinement procedure. Starting from an initial coarse grid, the Laplace solver is executed through a sequence of refinement steps (typically five or six steps in total), in which the grid density is doubled at each step. The converged solution at a given step is interpolated onto the refined grid and used as the initial guess for the subsequent step.

F. Electric-field evaluation on the conductor surfaces

We next describe how the electric field is evaluated from the numerically computed potential. After obtaining $\phi(\xi, \eta, \theta)$, we compute the electric field in physical space as $\mathbf{E} = -\nabla\phi$. To evaluate the physical-space derivatives, we first compute $\partial\phi/\partial\xi$ and $\partial\phi/\partial\eta$ on the coordinate grid and then transform them to physical-space derivatives using the Jacobian of the coordinate mapping.

For the tip surface ($\eta = \eta_T$), the normal field component is evaluated using a higher-accuracy one-sided boundary derivative to reduce discretization error. Specifically, instead of using a single-step finite difference at the boundary, we sample the potential at several grid points (seven points) along the η coordinate line in the vacuum region immediately adjacent to the tip surface (toward decreasing η at fixed ξ), and evaluate $\partial\phi/\partial\eta|_{\eta=\eta_T}$ using a one-sided finite-difference stencil (equivalently, polynomial interpolation followed by differentiation) [7]. Because the tip surface is an equipotential (Dirichlet boundary), the tangential derivative along the surface vanishes; accordingly, $\partial\phi/\partial\xi|_{\eta=\eta_T} = 0$.

The derivative information is then converted to the physical-space gradient components $(\partial\phi/\partial r, \partial\phi/\partial z)$ using the Jacobian of the mapping $r(\xi, \eta)$ and $z(\xi, \eta)$. Defining

$$\mathbf{J} \equiv \begin{pmatrix} r_\xi & r_\eta \\ z_\xi & z_\eta \end{pmatrix}, \qquad \mathbf{J}^{-1} = \begin{pmatrix} \xi_r & \xi_z \\ \eta_r & \eta_z \end{pmatrix}, \tag{42}$$

the chain rule gives

$$\begin{pmatrix} \partial\phi/\partial r \\ \partial\phi/\partial z \end{pmatrix} = \left(\mathbf{J}^{-1}\right)^T \begin{pmatrix} \partial\phi/\partial\xi \\ \partial\phi/\partial\eta \end{pmatrix} = \begin{pmatrix} \xi_r & \eta_r \\ \xi_z & \eta_z \end{pmatrix} \begin{pmatrix} \partial\phi/\partial\xi \\ \partial\phi/\partial\eta \end{pmatrix}. \tag{43}$$

Here, $r_\xi = \partial r/\partial\xi$, etc., follow from Eqs. (3) and (4). The resulting $\nabla\phi$ is perpendicular to the equipotential tip surface, and its magnitude gives the normal field component on the tip, $|E_n| = |\nabla\phi|$.

For the 2D calculations, the sample boundary at $\eta = 0$ is laterally uniform, so that the electric field at the sample plane has only the normal component. The normal field is obtained from a one-sided derivative along the η direction. Specifically, the potential is sampled along the η line starting from the Dirichlet boundary value at the surface and several adjacent vacuum nodes, and $\partial\phi/\partial\eta|_{\eta=0}$ is evaluated using a one-sided finite-difference stencil [7]. Using the local relation $z(\xi,\eta) = a(\xi + c)\eta$, this derivative is converted to the vertical derivative at the sample plane as

$$\left.\frac{\partial\phi}{\partial z}\right|_{z=0} = \frac{1}{a(\xi+c)}\left.\frac{\partial\phi}{\partial\eta}\right|_{\eta=0}, \tag{44}$$

which gives $E_z = -\left.\partial\phi/\partial z\right|_{z=0}$.

For the 3D calculations, in contrast, an arbitrary laterally varying surface potential $V_s(\xi,\theta)$ is prescribed at $\eta = 0$. The normal field component is evaluated in the same manner as in the 2D case, namely from a one-sided derivative along η followed by the transformation

$$\left.\frac{\partial\phi}{\partial z}\right|_{z=0} = \frac{1}{a(\xi+c)}\left.\frac{\partial\phi}{\partial\eta}\right|_{\eta=0}, \tag{45}$$

so that $E_z = -\left.\partial\phi/\partial z\right|_{z=0}$. However, because V_s varies laterally, tangential field components generally remain finite on the sample plane. In cylindrical coordinates, these are evaluated as

$$E_r = -\frac{\partial V_s}{\partial r}, \qquad E_\theta = -\frac{1}{r}\frac{\partial V_s}{\partial\theta}. \tag{46}$$

In the implementation, E_r is evaluated from finite differences on the nonuniform radial grid, whereas E_θ is obtained from a periodic finite difference in θ.

G. Maxwell-stress force evaluation

The electrostatic force is computed from the Maxwell stress on the conductor surfaces. For the tip side, the electrostatic pressure in vacuum is given by

$$p = \frac{1}{2}\varepsilon_0 E_n^2, \tag{47}$$

where E_n is the electric-field component normal to the surface. The vertical force is then obtained by integrating the pressure over the tip surface,

$$F_z = \iint p\, n_z\, dS, \tag{48}$$

where n_z is the z component of the unit normal vector and dS is the surface area element.

For the planar sample surface in the 2D calculations, no tangential field component is present, and the vertical traction reduces to the usual electrostatic pressure,

$$T_{zz} = \frac{\varepsilon_0}{2} E_z^2. \tag{49}$$

The corresponding sample-side force is therefore

$$F_z^{\text{sample}} = 2\pi \int_0^{r_{\max}} T_{zz}(r)\, r\, dr, \tag{50}$$

which is evaluated numerically on the discrete grid.

For the 3D calculations, because laterally varying surface potentials generally produce both normal and tangential electric-field components on the sample plane, the vertical component of the Maxwell stress is evaluated as

$$T_{zz} = \frac{\varepsilon_0}{2} \left(E_z^2 - E_r^2 - E_\theta^2 \right). \tag{51}$$

The total sample-side vertical force is then obtained by integrating T_{zz} over the sample surface,

$$F_z = \iint T_{zz}\, r\, dr\, d\theta. \tag{52}$$

Thus, unlike in the 2D case, the 3D force evaluation explicitly includes the contributions of both the normal and lateral electric-field components on the sample surface.

H. Internal consistency check of tip- and sample-side forces

As an internal consistency check (action–reaction), the mismatch between the forces obtained from the tip and sample surfaces is quantified as

$$\delta F \equiv \frac{2\left| |F_z^{\text{tip}}| - |F_z^{\text{sample}}| \right|}{|F_z^{\text{tip}}| + |F_z^{\text{sample}}|}. \tag{53}$$

We find that δF decreases upon refining the η-direction mesh, reflecting the sensitivity of the tip-side evaluation to the strongly localized field near the apex (note that $p \propto E_n^2$ amplifies

discretization-induced errors). As described above, the calculations use staged refinement; here we only summarize the practical choice of the baseline (coarsest-level) η-grid number $N_{\mathrm{v,in}}$. For tips with relatively large opening angles ($\alpha \geq 15^\circ$), $N_{\mathrm{v,in}} = 4$ or 8 is typically sufficient to achieve agreement between the tip- and sample-side force evaluations within a few percent, whereas for sharper tips ($\alpha < 15^\circ$), $N_{\mathrm{v,in}} \geq 16$ is generally required to reach a comparable level of agreement.

Importantly, when $N_{\mathrm{v,in}}$ is varied, the tip-side force F_z^{tip} changes substantially more than the sample-side force F_z^{sample}, while F_z^{sample} remains comparatively stable. This indicates that the residual mismatch is dominated by discretization sensitivity on the tip side, and that increasing the η resolution mainly reduces this tip-side contribution to the mismatch. In principle, the electrostatic force acting between the tip and sample can be evaluated from either the tip-side or sample-side stress integration alone. Therefore, in practice, it is not necessary to increase the grid resolution until F_z^{tip} fully matches F_z^{sample}. In the present calculations, to reduce computational cost in extensive parameter sweeps, we use a modest $N_{\mathrm{v,in}}$ and evaluate the force from the sample-side stress integration, while performing additional refinements only when needed to confirm the stability of F_z^{sample} and the consistency of the result.

I. Conversion from static STM setpoint distance to mean oscillation distance

In ultrahigh vacuum atomic force microscopy (AFM)/Kelvin probe force microscopy (KPFM) measurements, the tip–sample distance is often controlled by scanning tunneling microscopy (STM) feedback, i.e., by using tunneling current. However, in AFM/KPFM measurements, the tip is mechanically oscillated, and the tip–sample distance is therefore effectively regulated through the tunneling current averaged over the oscillation cycle. Consequently, for a given STM setpoint, the mean tip position during oscillatory operation is larger than the corresponding position in a non-oscillating (static) configuration.

In METALTIP, for convenience and practical parameterization, we use as the input parameter a nominal tip–sample separation s defined for the static (non-oscillating) STM case. This choice is convenient because the corresponding distance range is commonly used as an experimental reference (typically on the order of $\sim$0.7–1.0 nm under usual STM conditions), whereas directly specifying the mean distance during oscillatory operation would

require explicit amplitude-dependent correction. The mean tip position $\langle s \rangle$ used in the electrostatic potential and force calculations is then determined so that the oscillation-averaged tunneling current matches the tunneling current at the static reference distance s.

Assuming an exponential distance dependence of the tunneling current,

$$I \propto \exp(-2\kappa s), \tag{54}$$

and writing the instantaneous separation during FM operation as

$$s(t) = \langle s \rangle + A\cos(2\pi f_0 t), \tag{55}$$

the matching condition for the tunneling current is

$$\langle \exp[-2\kappa\,(\langle s \rangle + A\cos\omega t)] \rangle = \exp(-2\kappa s), \tag{56}$$

where $\omega = 2\pi f_0$. The left-hand side can be separated into the contribution from the mean tip position and the oscillatory contribution:

$$\exp(-2\kappa\langle s \rangle)\,\langle \exp[-2\kappa A\cos\omega t] \rangle = \exp(-2\kappa s). \tag{57}$$

Using the integral representation of the modified Bessel function,

$$I_0(x) = \frac{1}{2\pi}\int_0^{2\pi} \exp(x\cos\theta)\,d\theta, \tag{58}$$

and noting that $I_0(-x) = I_0(x)$, the oscillation average is given by

$$\langle \exp[-2\kappa A\cos\omega t] \rangle = I_0(2\kappa A). \tag{59}$$

The current-matching condition therefore becomes

$$\exp(-2\kappa\langle s \rangle) I_0(2\kappa A) = \exp(-2\kappa s), \tag{60}$$

which yields

$$\langle s \rangle = s + \frac{1}{2\kappa}\ln[I_0(2\kappa A)]\,, \tag{61}$$

where I_0 is the modified Bessel function of the first kind. In the simulations, $\langle s \rangle$ is used as the mean tip position for evaluating electrostatic quantities and oscillation-averaged observables such as Δf.

II. SUPPLEMENTARY NOTE II: SAMPLE PREPARATION

A Cu(111) single-crystal substrate was cleaned by repeated cycles of Ar^+-ion sputtering and annealing. After cleaning, the sample was transferred to the cryostat of the scanning probe microscopy (SPM) chamber and cooled to ∼78 K. It was then transferred to the room-temperature preparation chamber, where NaCl was deposited immediately by thermal evaporation from a glass crucible heated to 580 °C for 3 min. After deposition, the sample was left in the preparation chamber for 20 min and was then transferred back to the SPM chamber. This procedure resulted in the formation of rectangular-shaped NaCl islands.

III. SUPPLEMENTARY FIGURES

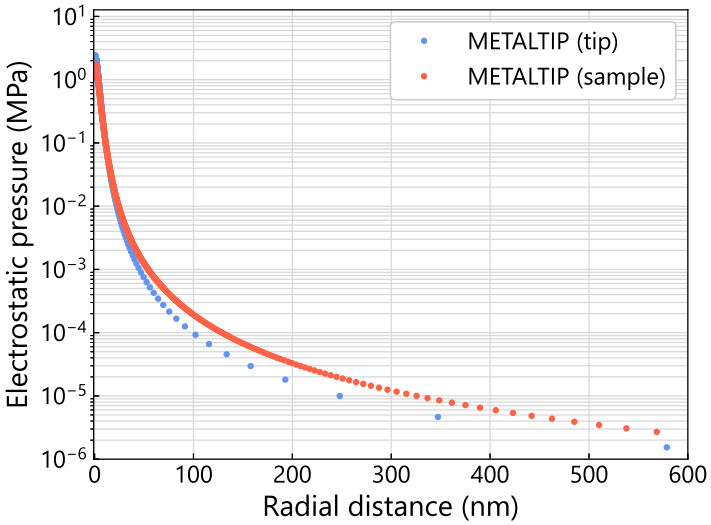

FIG. S2: Radial dependence of the electrostatic pressure on a logarithmic vertical scale, evaluated on the tip surface (blue circles) and on the sample surface (red circles) for a sharp hyperbolic tip geometry ($R = 10$ nm, $\alpha = 10°$) at an applied bias of 1.0 V. Near the apex region, the pressure is larger on the tip side, whereas the weak long-range tail is more pronounced on the sample side. Although this tail is small in magnitude, it contributes to the total force through the area-weighted surface integral ($\propto r\, dr$). Therefore, a sufficiently large radial integration range is required to obtain quantitative agreement between the tip-side and sample-side force integrations (typically within $\sim$5%).

Alt text: Log-scale radial profiles of electrostatic pressure on the tip and sample surfaces for a sharp hyperbolic tip. The tip-side pressure is larger near the apex, whereas the sample-side pressure shows a larger long-range tail at larger radial distances, indicating different spatial weightings of the two surface integrations.

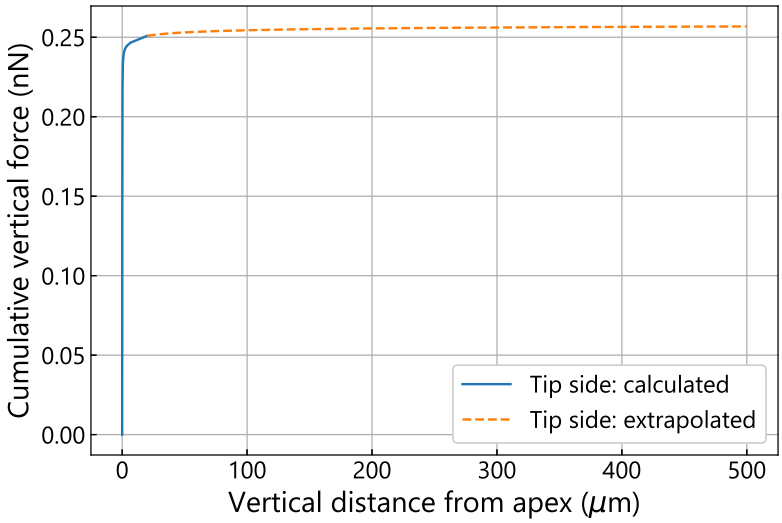

FIG. S3: Cumulative vertical electrostatic force on the tip side as a function of the vertical distance from the apex. The solid line shows the force obtained by integrating the calculated tip-side electrostatic pressure within the computational domain, which extends to approximately 18 μm from the apex for a full opening angle of 10°. The dashed line shows an extrapolation of the outer tail of the pressure distribution to 500 μm, chosen to cover the typical length scale of the actual tip used in self-sensing force sensors. The cumulative force is already close to saturation within the modeled hyperbolic-tip region, indicating that the additional contribution from more distant metallic parts of the probe is expected to be small.

Alt text: Cumulative vertical electrostatic force plotted as a function of distance along the z direction from the tip apex. The curve approaches saturation within the modeled hyperbolic-tip region, supporting the assumption that electrostatic contributions from more distant probe parts are small.

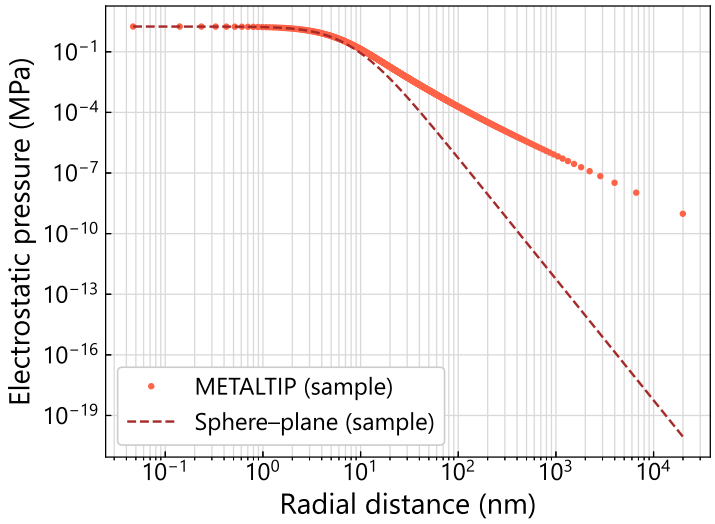

FIG. S4: Logarithmic-scale comparison of the sample-side electrostatic pressure profile calculated with METALTIP (solid circles) and the analytical sphere–plane model (dashed line). The two profiles agree well in the near-apex region (small r), where the local apex curvature dominates the electrostatic response. At larger radial distances, however, the METALTIP result increasingly deviates from the sphere–plane prediction, indicating additional long-range contributions from the hyperbolic tip shank, which are included in METALTIP but absent in the idealized sphere–plane geometry.

Alt text: Log-scale comparison of sample-side electrostatic pressure calculated by METALTIP and by the analytical sphere–plane model. The two profiles agree near the apex but deviate at larger radial distances because METALTIP includes long-range contributions from the hyperbolic shank.

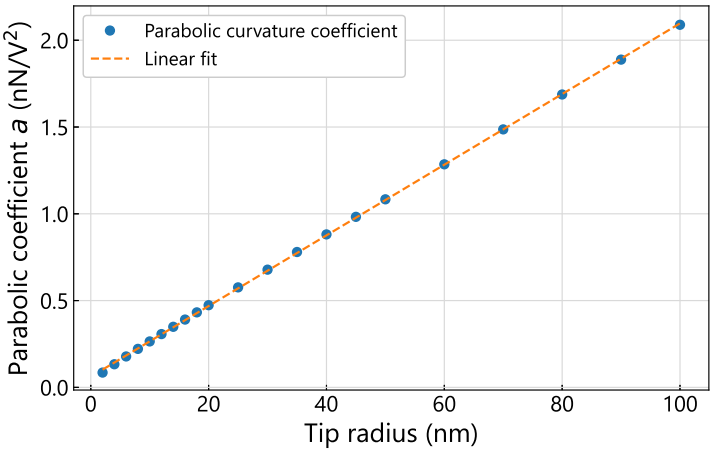

FIG. S5: Dependence of the parabolic curvature coefficient a on the tip radius R. For each R, the coefficient a was obtained by fitting the calculated F–U curve with $F(U) = a(U - U_0)^2 + F_0$. The resulting $a(R)$ values (solid circles) were fitted using a linear function, $a(R) = mR + b$, over the full range $R = 2$–100 nm (dashed line). The linear fit yielded a coefficient of determination of $R^2_{\mathrm{lin}} = 0.99990$. The maximum relative deviation from the fit was 16.6%, which occurred at the smallest radius, $R = 2$ nm, while the root-mean-square relative deviation over the full range was 4.0%. This behavior is consistent with the near-field scaling expected for the tip–sample electrostatic response for fixed tip-geometry parameters other than R.

Alt text: Parabolic curvature coefficient a plotted as a function of tip radius R. The coefficient increases almost linearly with R over the range $R = 2$–100 nm, with small deviations from the linear fit except at the smallest radius.

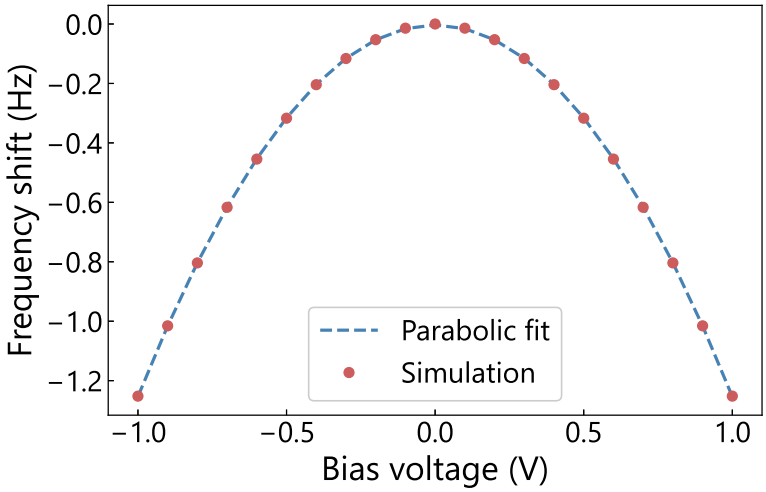

FIG. S6: Bias dependence of the frequency shift (Δf–U curve) calculated for the same tip–sample geometry as in Fig. 3 of the main article. Solid circles denote the calculated values, and the dashed line shows a parabolic fit.

Alt text: Simulated frequency-shift–bias curve for a laterally homogeneous conducting surface. The calculated Δf–U data follow a parabolic dependence on bias voltage.

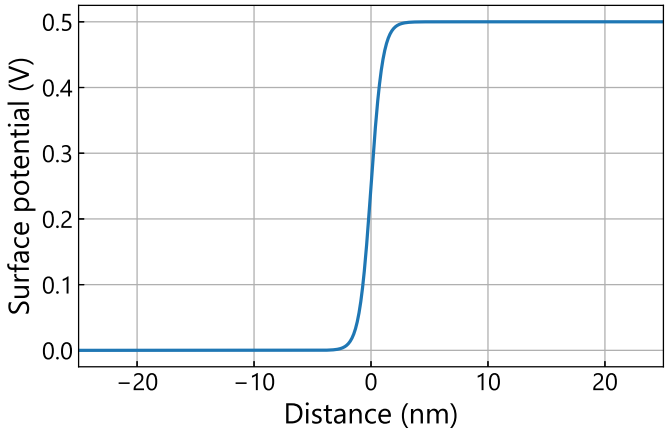

FIG. S7: Surface-potential profile used for the single-step model. The surface potential is given by $V_{\mathrm{s}}(x) = \frac{\mathrm{CPD_{diff}}}{2}\left[1 + \tanh\left(\frac{x}{w_{\mathrm{interface}}}\right)\right]$, which describes a smooth step from 0 to $\mathrm{CPD_{diff}}$ centered at $x = 0$. Here, $\mathrm{CPD_{diff}} = 0.5$ V and the interfacial width parameter was set to $w_{\mathrm{interface}} = 1.0$ nm.

Alt text: Smooth surface-potential step used in the single-step model. The potential changes from 0 to $\mathrm{CPD_{diff}} = 0.5$ V across the interface with a smoothing width of $w_{\mathrm{interface}} = 1.0$ nm.

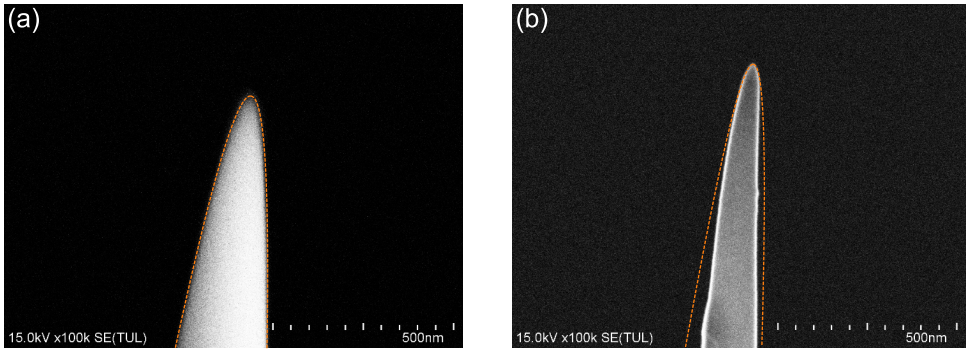

FIG. S8: Representative scanning electron microscopy images of as-provided tungsten (W) tips (Unisoku), together with single-hyperbola fits to the outer tip profile (orange dashed curves). (a) Example of a tip whose outer profile is well reproduced by a single hyperbolic curve over a broad axial range from the apex; the fit shown uses $R = 10$ nm and $\alpha = 7°$. (b) Example of a tip for which a single hyperbolic curve cannot simultaneously reproduce the near-apex region and the shank profile within the fitting window; the fit shown uses $R = 6$ nm and $\alpha = 6°$. For this tip, further decreasing α does not substantially improve the fit to the shank profile within the fitting window.

Alt text: Scanning electron microscopy images of tungsten tips with hyperbolic fits to the outer profiles. One tip is well reproduced by a single hyperbola, whereas another shows a mismatch between the near-apex region and the shank profile.

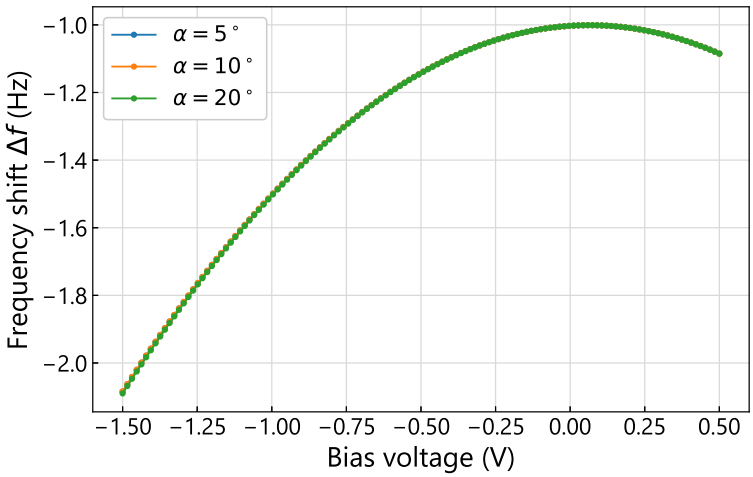

FIG. S9: Simulated Δf–U curves calculated for different full shank opening angles, $\alpha = 5°$, $10°$, and $20°$. The CPD value and bias-voltage range were set to the same conditions as those used for the comparison with the experimental Δf–U curve in the main text. The frequency-shift response shows only a weak dependence on α in this range, supporting the use of $\alpha = 10°$ as a representative fixed opening angle in the fitting simulations.

Alt text: Simulated Δf–U curves for full shank opening angles of $\alpha = 5°$, $10°$, and $20°$. The curves differ only weakly, supporting the use of $\alpha = 10°$ as a representative fixed opening angle in the fitting simulations.

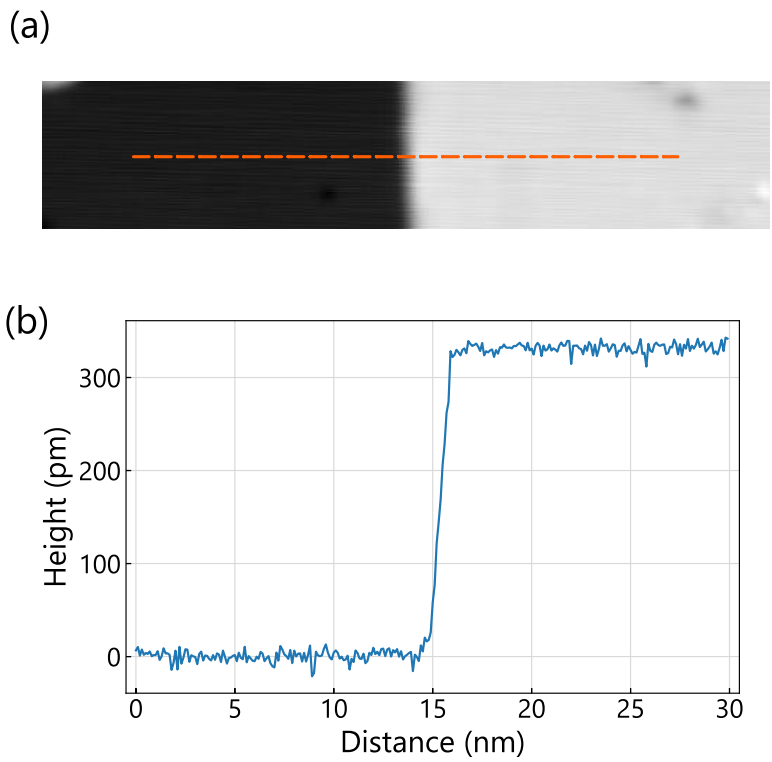

FIG. S10: STM-mode topography and corresponding line profile of the NaCl/Cu(111) interface region used for acquiring the interfacial CPD profile for fitting. (a) Representative STM topographic image of the measurement area containing a partially NaCl-covered Cu(111) surface. The orange dashed line indicates the position at which the line profile across the NaCl/Cu(111) interface was acquired. The grayscale corresponds to a height range of 0–400 pm. (b) Line profile taken along the dashed line in (a), showing an apparent step height of approximately 320 pm between the bare Cu(111) terrace and the NaCl-covered terrace, consistent with a two-monolayer NaCl film.

Alt text: STM topographic image and line profile of the NaCl/Cu(111) interface region used for CPD-profile fitting. The line profile shows an apparent height difference of approximately 320 pm between the Cu(111) terrace and the two-monolayer NaCl island.

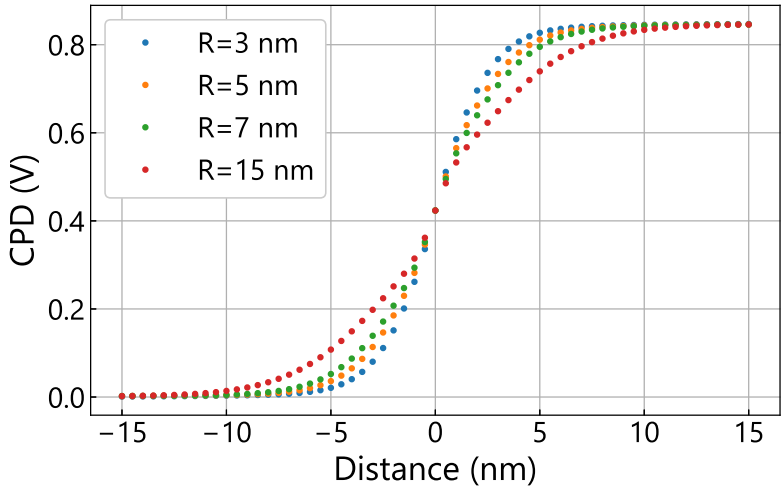

FIG. S11: Simulated CPD profiles across a surface-potential boundary for different tip radii, $R = 3$, 5, 7, and 15 nm. As R increases, the interfacial transition becomes broader, whereas sharper tips yield a narrower CPD transition. This demonstrates that the width of the simulated CPD profile is strongly governed by the electrically effective tip radius.

Alt text: Simulated CPD profiles across a surface-potential boundary for different tip radii. Larger tip radii produce broader interfacial transitions, showing that the CPD-profile width is mainly governed by the tip radius.

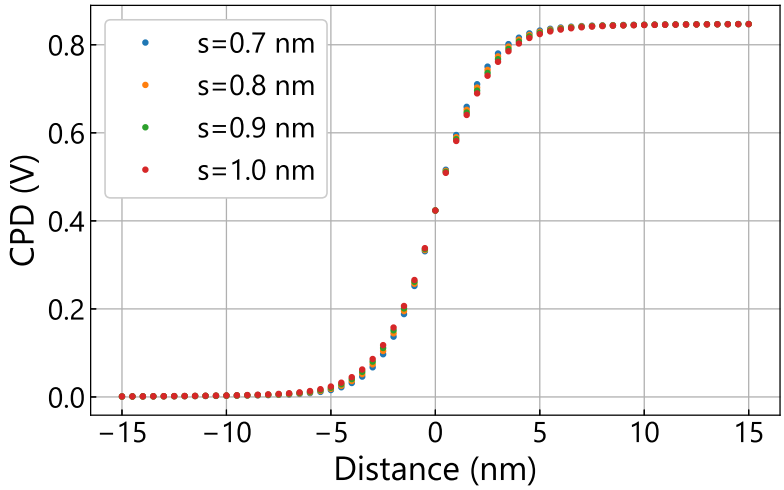

FIG. S12: Simulated CPD profiles across a surface-potential boundary for several tip–sample separations, $s = 0.7$, 0.8, 0.9, and 1.0 nm. Over this physically reasonable range for STM-mode regulation, the CPD-profile shape shows no appreciable dependence on s, indicating that the interfacial broadening is governed primarily by the electrically effective tip radius rather than by the operating separation.

Alt text: Simulated CPD profiles for tip–sample separations from $s = 0.7$ to 1.0 nm. The profile shape changes very little over this range, indicating that the interfacial broadening is much less sensitive to s than to the effective tip radius.

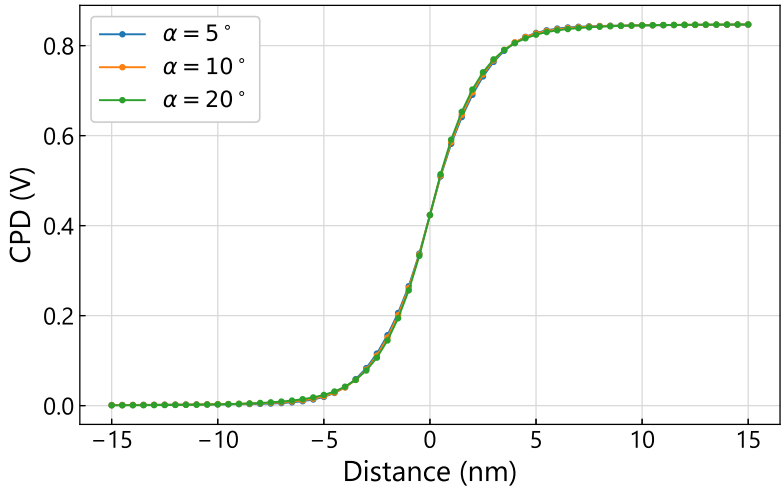

FIG. S13: Simulated CPD profiles across a lateral surface-potential step calculated for different full shank opening angles, $\alpha = 5°$, $10°$, and $20°$. The potential difference between the two regions was set to the experimentally determined CPD difference, and the tip–sample geometry parameters were fixed at $R = 3.0$ nm and $s = 0.9$ nm, except for α. The CPD-profile width changes only weakly over this range of α, indicating that the interfacial broadening is much less sensitive to the shank opening angle than to the effective tip radius R under the present small-separation conditions.

Alt text: Simulated CPD profiles for full shank opening angles of $\alpha = 5°$, $10°$, and $20°$. The CPD-profile width changes only weakly with α, indicating that the broadening is less sensitive to the opening angle than to the effective tip radius.

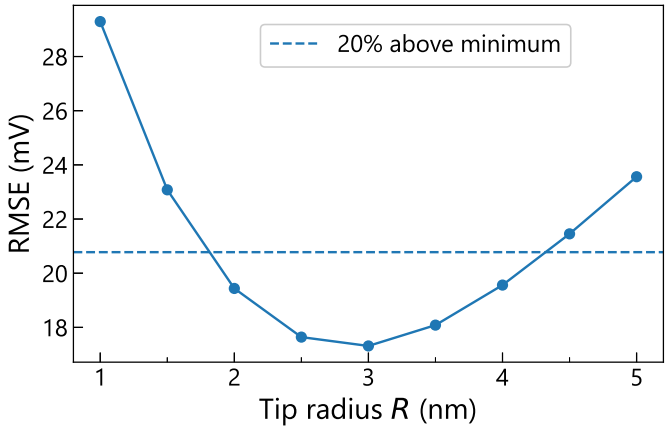

FIG. S14: Root mean square error (RMSE) between the experimental and simulated CPD profiles plotted as a function of the tip radius R. The simulated CPD profiles were calculated for fixed $s = 0.9$ nm and $\alpha = 10°$, and compared with the experimental profile after applying the same interface-position correction as used in the main-text fitting. The RMSE exhibits a shallow minimum around $R = 2.5$–3.0 nm. The dashed line marks the 20%-above-minimum tolerance level, corresponding to an acceptable range of approximately $R = 2.0$–4.0 nm.

Alt text: Root-mean-square error between experimental and simulated CPD profiles plotted as a function of tip radius R. The RMSE has a shallow minimum around $R = 2.5$–3.0 nm, and the 20%-above-minimum criterion gives an acceptable range of approximately $R = 2.0$–4.0 nm.

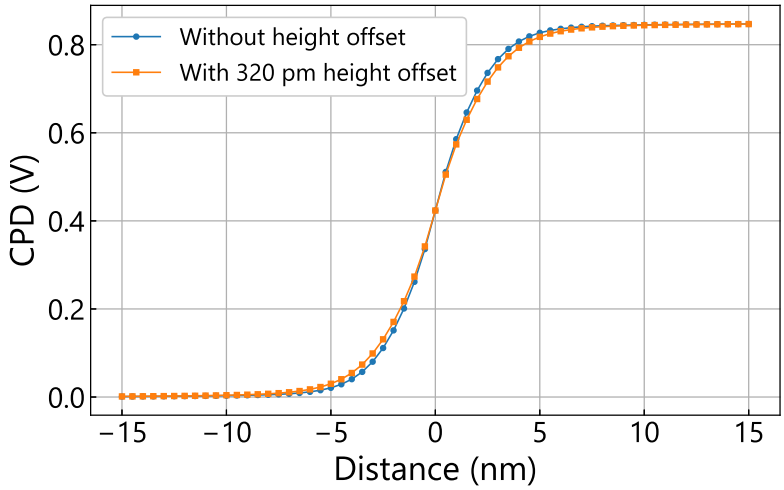

FIG. S15: Simulated CPD profiles calculated using the flat-surface model for $R = 3.0$ nm and $\alpha = 10°$, without and with a +320 pm offset in the tip–sample separation. The offset corresponds to the apparent height difference between the Cu(111) terrace and the 2 ML NaCl island in the experiment. Because both profiles were calculated for a geometrically flat sample surface, the offset calculation should be regarded as a sensitivity test for the neglected height difference rather than as a full simulation of the non-flat boundary geometry. Nevertheless, the small difference between the two profiles indicates that the flat-surface approximation does not substantially affect the CPD-profile broadening used for the tip-radius extraction.

Alt text: Simulated CPD profiles calculated with and without a +320 pm offset in the tip–sample separation. The two profiles differ only slightly, indicating that the neglected apparent height difference between Cu(111) and two-monolayer NaCl does not substantially affect the CPD-profile broadening.

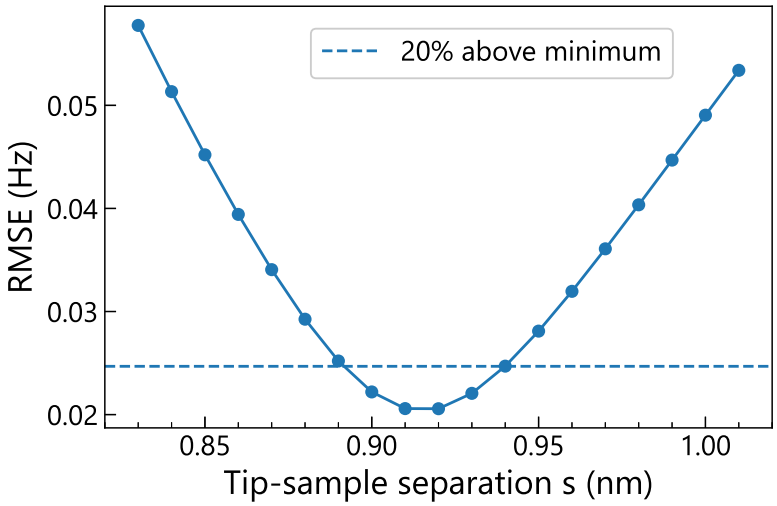

FIG. S16: Root-mean-square error (RMSE) between the experimental and simulated Δf–U curves plotted as a function of the static STM-mode tip–sample separation s. The simulated curves were calculated for fixed $R = 3.0$ nm and $\alpha = 10°$, and each curve was compared with the experimental data after interpolation onto the experimental bias points. The RMSE shows a clear minimum around $s = 0.91$–0.92 nm. The dashed line indicates a tolerance level 20% above the minimum RMSE, giving an acceptable range of approximately $s = 0.90$–0.93 nm.

Alt text: Root-mean-square error between experimental and simulated Δf–U curves plotted as a function of static STM-mode tip–sample separation s. The RMSE is minimized around $s = 0.91$–0.92 nm, with an acceptable range of approximately $s = 0.90$–0.93 nm.

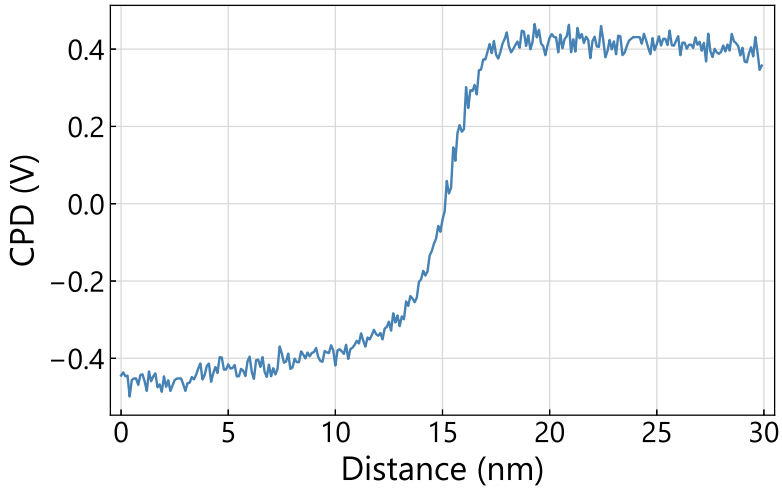

FIG. S17: Additional examples of CPD profiles measured across the NaCl/Cu(111) interface. Although the CPD changed sharply at the interface, some profiles did not become fully flat in regions far from the boundary. One possible interpretation is that these tips remained relatively sharp near the apex but became thicker in the outer region than expected from the ideal hyperbolic geometry assumed in the model.

Alt text: Additional experimental CPD profiles measured across NaCl/Cu(111) interfaces. Some profiles show a sharp interfacial change but do not become fully flat far from the boundary, suggesting deviations of the actual tip shape from the ideal hyperbolic model.

---

[1] R. M. Feenstra, Journal of Vacuum Science & Technology B **21**, 2080 (2003).

[2] R. M. Feenstra, S. Gaan, G. Meyer, and K.-H. Rieder, Physical Review B **71**, 125316 (2005).

[3] R. M. Feenstra, Y. Dong, M. P. Semtsiv, and W. T. Masselink, Nanotechnology **18**, 044015 (2007).

[4] Y. Dong, R. M. Feenstra, M. P. Semtsiv, and W. T. Masselink, Journal of Applied Physics **103**, 073704 (2008).

[5] N. Ishida, K. Sueoka, and R. M. Feenstra, Physical Review B **80**, 075320 (2009).

[6] S. Gaan, G. He, R. M. Feenstra, J. Walker, and E. Towe, Journal of Applied Physics **108**, 114315 (2010).

[7] B. Fornberg, SIAM Review **40**, 685 (1998).